UAV icing: Development of an ice protection system for the propeller of a small UAV

Nicolas Carlo Müller [a,b,*], Bogdan Løw-Hansen [a,b], Kasper Trolle Borup [b], Richard Hann [a,b,*]

[a] *Norwegian University of Sciences and Technology, Institutt for teknisk kybernetikk, 7491 Trondheim, Norway*
[b] *UBIQ Aerospace AS, Krambugata 2, Trondheim, Norway*

ARTICLE INFO

ABSTRACT

Atmospheric icing, also called in-flight icing, is a common hazard for the operation of uncrewed aerial vehicles (UAVs). With the background of a growing commercial and military market of small and medium-sized drones and the developments in the urban air mobility markets, protecting the propellers of UAVs against icing has become a pivotal technology to unlock the potential of these markets. The propellers and rotors accumulate ice faster than the UAVs' wings and airframe. This ice accumulation leads to aerodynamic degradation, making the protection of the propeller key for the operation of UAVs in conditions with potential icing. In this work, an electro-thermal ice protection system is developed for a propeller of a small UAV, with a propeller diameter of 53 cm or 21 inch. For the design of the system, the required anti-icing heat fluxes were calculated using icing computational fluid dynamics (CFD) analysis. Carbon fibre-based heating elements were integrated into the structure of the propeller. This propeller was tested in an icing wind tunnel at −5 °C, −10 °C, and −15 °C. The tests were performed with a rotation rate representative for a medium-sized UAV of 4200 rpm. The liquid water content of the wind tunnel was 0.44 g/m^3. It prevented the performance penalties from ice accretion at temperatures of −5 °C. At lower temperatures, the propeller IPS could limit the ice accretion on the propeller, thus allowing it to retain its ability to create thrust. The results showed a requirement for a significantly higher heat flux than predicted by the CFD analysis. This work is the first step in developing a mature ice protection system for the propellers and rotors of medium-sized UAVs and to enable all-weather operations.

1. Introduction

Atmospheric in-flight icing is an essential topic in the development of uncrewed (or unmanned) aerial systems (UAVs), also called remotely piloted aircraft systems (RPAS), or drones. Those systems are used in many commercial, military and search and rescue (SAR) applications (Shakhatreh et al., 2019). In many of those applications, the UAV must operate with high availability for a reliable and successful operation (Shakhatreh et al., 2019). One factor limiting the availability of a UAV is adverse weather (Gao et al., 2021). One typical adverse weather condition UAVs face is atmospheric icing (Cao et al., 2018; Hann and Johansen, 2020). If the UAV is flying through a cloud containing supercooled droplets, impinging droplets on the surface freeze upon contact. This ice accretion on the UAV typically has negative impacts on

the aerodynamic performance of the UAV (Szilder and Yuan, 2017). Ice accumulates on the airfoil and changes the aerodynamic shape, leading to a decrease in the ability of the wings to generate lift and an increase in the drag of the aircraft (Bragg et al., 2005). The mass of the accumulated ice increases the weight of the UAV (Szilder and Yuan, 2017). Typically, this is compensated by increasing the thrust from the propeller. This would overcome the increased drag. Most small and medium-sized fixed-wing UAVs use a propeller for propulsion of the UAV (Adamski, 2017). Propellers are also susceptible to icing and can quickly lose substantial aerodynamic performance due to icing (Liu et al., 2018). Due to typically smaller size and high relative air speeds (rotation), propellers are more sensitive to icing compared to wings (Müller et al., 2021; Hann and Johansen, 2021). Since the thrust generated by the propeller is essential for sustaining the flight of the UAV, ice accretion on

the propeller of a UAV is a critical issue for the operation of UAVs in icing conditions.

The impact of icing conditions on the performance of an aircraft is comparatively well understood for manned aviation (Cao et al., 2018; Bragg et al., 2005). Icing on rotating aerodynamic surfaces has been investigated for the propellers of manned aviation aircraft and the rotors of helicopters (Zhao et al., 2016; Cao and Chen, 2010) and wind turbines (Hochart et al., 2008; Yirtici et al., 2019). The icing on UAVs has only recently become a more active research area (Hann and Johansen, 2020). A significant part of this research focuses on the icing UAV airfoils (Szilder and McIlwain, 2011; Fajt et al., 2019; Hann et al., 2020; Williams et al., 2017). But in-flight icing does also affect other parts of the UAV, like for example the propellers or rotors. The ice accretion on the rotor or propeller can lead to a rapid loss of performance of the propeller or rotor (Liu et al., 2018). In icing wind tunnel experiments, it has been shown that ice accretion on propellers will decrease the propeller's thrust and increase the power required to run the propeller (Liu et al., 2018; Liu et al., 2019; Müller et al., 2021). This rapid thrust decrease can quickly lead to a loss of control of the UAV, especially for multi-rotor UAVs, which rely on the thrust of the rotors for the lift as well as the control (Yan et al., 2019). This would limit the operational envelope of UAVs as they would have to avoid icing conditions (Peck et al., 2020).

A special issue for the icing on rotating parts like propellers and rotors is the centrifugal force created by the rotation. This leads to ice shedding (Nilamdeen et al., 2019). Ice shedding describes the process when a part of the accumulated ice breaks off the propeller because the adhesion forces between the propeller and the ice are not strong enough to keep the ice on the propeller. Ice-shedding will recover parts of the performance loss of the propeller (Müller and Hann, 2022), but the ice fragment breaking of the propeller could also be a danger to the UAV. If the ice breaks off on a single blade of the propeller, an imbalance in the mass of the propeller is created, which induces strong vibrations in the system. Additionally, the aerodynamic forces will also be uneven between the blades further increasing the forces acting on the system. Lastly, the fragments might impact other parts of the UAVs and cause damage to those parts.

One solution to the problem of ice accretion on the propellers and rotors of UAVs is using ice protection systems (IPS) (Thomas et al., 1996). These are systems developed to mitigate the danger of ice accumulation on aircraft. There are two different operational concepts for ice protection systems. Anti-icing systems prevent ice accretion continuously, while de-icing systems allow for limited amounts of ice to accrete and then remove the ice periodically (Thomas et al., 1996). One key design challenge when developing an IPS for a UAV is the limited power available (Hann and Johansen, 2020). Manned aviation can often use the heat produced by the engine in the form of bleed air from the engine (Papadakis et al., 2012), or using systems like pneumatic de-icing boots to remove ice from the wing (Thomas et al., 1996). UAVs, especially those powered by electric motors, are limited by the amount of electric energy and strict weight requirements (Hann and Johansen, 2020). Possible IPS for the rotors of UAVs include the use of special surface coatings or an electro-thermal system. In an electro-thermal IPS, the electric energy is converted into heat and then used to protect the wing from ice accretion (Thomas et al., 1996).

Liu et al. (2018) have analysed the effects of superhydrophobic coatings, which reduce the adhesion of water droplets to the surface of the propeller. Compared to the untreated propeller, the coated propeller showed a significant reduction in the additional power consumption required to turn the propeller of 70% at temperatures of -5 °C. The thrust loss was reduced to 75%. This behaviour was observed to be due to a reduction in the accumulated ice mass outside of the impingement zone of the propeller and faster ice shedding. In a follow-up study by Han et al. (2022), the effectiveness of different surface coatings was compared in glaze and rime conditions. In this study, it was observed that surface coatings aiming at reducing the adhesion forces of the ice

could perform well in glaze and rime conditions. In contrast, super-hydrophobic coatings did not show a change in the ice accretion in rime conditions compared to the uncoated propeller. However, the used coating increased the ice adhesion and thus showed an increase in the ice accretion compared to the uncoated propeller.

Villeneuve et al. (2022) have researched the effect of multiple commercially available coatings on a scaled rotor of a small UAV. In their test at -12 °C, they discovered that only one of the tested coatings was able to reduce the ice accretion on the propeller to a level that would enable the UAV to continue to hover, but with a 28% reduction in the thrust and a 50% increase in torque.

Laroche et al. (2021) have developed a method of modifying the surface of metallic alloys to create hydrophobic and ice-phobic properties, which promise longer durability. In Alamri et al. (2020), Alamri et al. postulate the use of those surfaces to improve the efficiency of thermal IPS systems by combining thermal IPS with ice-phobic surfaces.

IPS have been successfully developed for the wings of UAVs (Hann et al., 2019; Wallisch and Hann, 2022). A rotor with an IPS has been developed by Karpen et al. (2022). In this design, a rotor of a multi-rotor UAV was covered with an electrical heater that consisted of three different heater zones over the propeller. These zones were of a fixed heat flux ratio between the zones given by their relative electrical resistance. The heat flux ratio describes the relative heat flux two different heater zones will provide and is usually fixed unless the zones can be controlled separately. A carbon-based paint was used as a heater. This paint provided a passive temperature control by the strong positive temperature gradient of the paint at 60 °C. Power was provided to the system by a supercapacitor included in the hub of the rotor. This rotor protected the propeller from icing in glaze at 0 °C conditions for 15 min until the supercapacitor's energy was depleted. In rime conditions at -10 °C, the system could not keep the propeller ice-free, but it increased the frequency of ice shedding events, reducing icing penalties overall.

On rotating parts, additional challenges compared to the wing arise concerning the development of an IPS. Here the required heat flux is now also dependent on the radial position along the propeller, based on the changing flow conditions along the radius of the propeller (Samad et al., 2021). Furthermore, the reduced size compared to wings also poses a challenge with the integration of the heating element and the small tolerances during the assembly. Another issue is the power delivery to the rotating propeller. One solution is to provide the rotor with an independent power source in the hub of the rotor (Karpen et al., 2022) or supply it with energy from the UAV through the motor, as done by Meteomatics (2017) in their developed electro-thermal IPS for a rotor of a small multirotor UAV.

The objective of this work is to develop an IPS for a propeller of a small UAV with a wingspan of 3 m and a mass of 25 kg. This propeller IPS is then tested in an icing wind tunnel to verify its performance. The required anti-icing loads are estimated with numerical simulations, and the results are compared to the experimental data. In the chosen IPS design, the electric power to the system is provided by the UAV through the motor. The IPS uses heating elements that are implemented into the propeller structure. The system was tested in an icing wind tunnel (IWT), with measurements of the thrust and torque of the motor. The propellers were tested at different temperatures from -5 °C to -15 °C. The liquid water content (LWC) of the air was 0.44 g/m^3 and the mean volumetric diameter (MVD) of the droplets was 24.2 μm. The total power the IPS has been supplied with was varied to see the response of the IPS at multiple power levels. The system has been developed as a part of the UIBQ Aerospace D•ICE system in collaboration with Mejzlik Propellers.

This paper aims to develop a key technology that will support the use of UAVs in icing conditions. This will increase the viability of UAVs for commercial applications and will expand the use the UAVs have in cold climates. Especially for uses with strict requirements on the availability of the system, such as, for example, SAR operations.
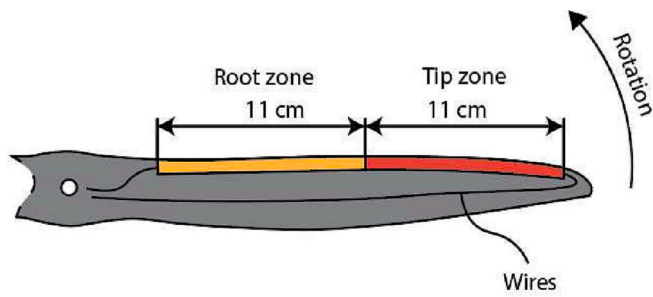
Fig. 1. Ice protection system layout on the propeller as seen from the top of the propeller.
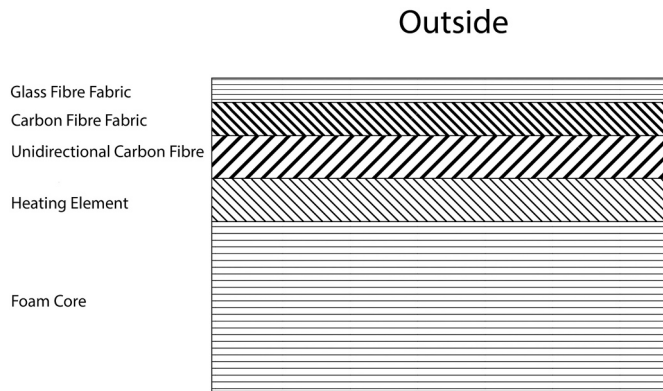
Fig. 2. Layup plan of the heated propeller at the areas of the heating element.

2. Methods

In this section, the design of the propeller IPS and the testing methods are presented. First, the design approach of the propeller IPS is presented, and then the experimental testing methods are presented, followed by the numerical methods used in the paper.

2.1. Design of the IPS

A representative of the propeller for a small fixed-wing UAV with a wingspan of about 3 meters was selected. The chosen propeller is the 21x13 EL propeller by Mejzlik (2021) and has a diameter of 0.53 m or 21 inch. The propeller is manufactured from a carbon fibre composites part with a foam core. The design of the IPS was based on numerical simulations, which will be presented later. The chosen design has a heating element on each blade consisting of a unidirectional carbon fibre roving on the leading edge. The 7 mm wide heating element covers the leading edge and a small part of the top surface of the propeller. The layout of the heating zones can be seen in Fig. 1. The heating element is placed on the leading edge of the propeller and covers the area of the propeller that is outside of the spinner. The heating element is designed with two areas of variable material thickness. The goal is to adapt the heat flux to the changing heat flux requirements along the propeller radius. The heating element in the root zone has twice the thickness compared to the tip zone. This variation in thickness allows the specification of two different heat fluxes along the span of the propeller to capture the increasing heat flux requirements from the root to the tip. Each heating zone has a length of 11 cm. The tip heating zone ends two cm away from the tip of the propeller to allow for the integration of the electrical connection to the heating zone. The heating zones are connected to the wires with a resin containing silver additives to allow for the electrical connection.

The composite layup of the propeller can be seen in Fig. 2. The heating element is placed on the polyurethane foam core. A layer of a glass fibre fabric is used to insulate the heating element. This is followed by a layer of unidirectional carbon and one layer of carbon fabric. The top layer is another layer of glass fibre fabric. The resin used during the propeller manufacturing has a glass transition temperature of 80 °C.

During the manufacturing, the heating zones were attached to the foam core of the propeller with a resin with a high heat deflection temperature of 160 °C. The cables for the electrical connections were placed in grooves on the foam core. During the final manufacturing process, first, the outer layers of the propeller carbon layup were placed in the mould. The foam core with the heating element was the last element placed before both mould halves were closed. Both propeller moulds were then compressed using a pneumatic system and heated to 60 °C to cure the resin. This temperature also marks the maximum temperature limit of the structure during IPS operation.

2.2. Experimental setup

The experiments were performed at an icing wind tunnel at the VTT Technical Research Centre of Finland in Helsinki (Tiihonen et al., 2016). This is an open loop wind tunnel capable of reaching wind speeds of 50 m/s and creating icing conditions down to −25 °C. The test section has a
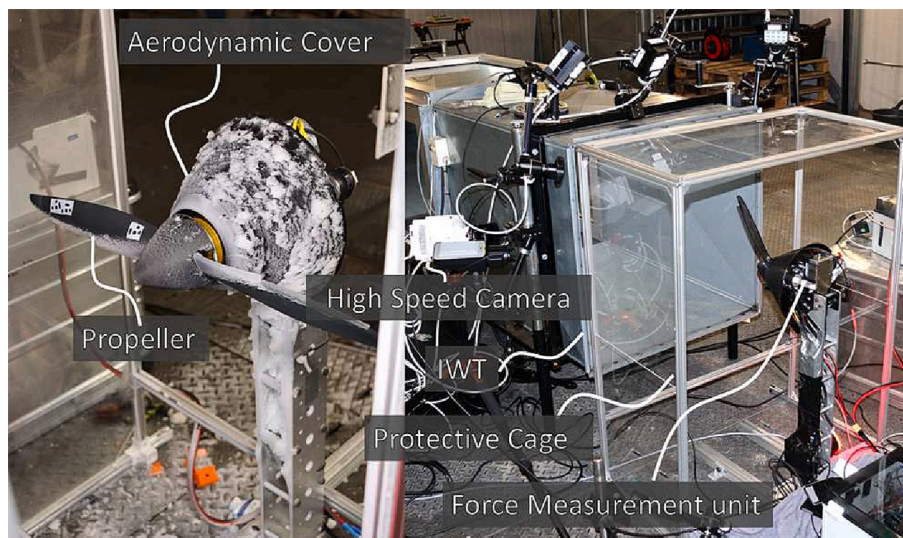
Fig. 3. Test equipment as installed in the IWT.

Table 1
Temperature calibration values of the RC Benchmark Series 1780 test-bench.

Temperature	Measured torque	Factor
21 °C	1.97 Nm	1.00
−2 °C	1.95 Nm	0.99
−5 °C	1.89 Nm	0.96
−10 °C	1.85 Nm	0.94
−15 °C	1.80 Nm	0.92

Table 2
Range of test conditions in the IWT during the test campaign.

Variable	Minimum	Maximum	Variability
T	−5 °C	−15 °C	±0.3 °C
Runtime	240 s	600 s	±5 s
IPS Power	0 W	250 W	±10 W
Rotation rate	4200 rpm	-	±10 rpm
LWC	0.44 g/m^3	-	±0.05 g/m^3
MVD	24.2 μm	-	±0.4 μm
Air velocity	25 m/s	-	±2.5 m/s

square cross-section with a width of 70 cm). The LWC of the wind tunnel is calibrated at the beginning of each experimental test campaign using a rotating cylinder (SAE International, 2015).

In Fig. 3, the test setup in the IWT is shown. The dynamometer "RC-Test bench 1780" from Tyto Robotics (2023) was used to measure the propeller's thrust and torque at 40 Hz. It send commands to the Kontronik Jive PRO 80 + HV (Kontronik, 2023) electronic speed controller (ESC). The rotation rate of the propeller was measured using an infrared sensor and a reflector on the motor. A custom-made conical cover protects the motor and the force measurement areas from ice accretion. This cover mounted on the test setup such that the forces on it are not recorded by the dynamometer. The motor rotation rate is kept constant during the experiment using a Javascript macro run on the control software by Tyto robotics.

An Axi 5345 HD 3D Extreme V2 motor is placed on the dynanometer (AXI MODEL MOTORS, 2023). The motor has been modified to allow an electrical connection through a slipring to the heating system in the propeller. This modification uses a proprietary system developed by UBIQ Aerospace that uses slip rings to connect the propeller to the electrical supply inside the UAV. The power was regulated using a control board and pulse width modulation (PWM).

A Phantom VEO 710L high-speed camera system is used to analyse the ice accretion on the propeller (Vision Research Inc., 2023). It is synchronised with the rotation of the propeller. This is triggered by the signal from the optical rotation rate sensor of the dynamometer. This signal is processed by an Arduino Uno Wifi Rev 2.0. The Arduino controls the timing of the high-speed camera. Four MultiLED QT lights are used to illuminate the propeller (GSVITEC, 2023). They are controlled by a MultiLED G8 controller (GSVITEC, 2023). The lights are synchronised with the high-speed camera. The lights are only illuminated for 15 μs per rotation to avoid influences of the lights on the propeller's ice accretion. The duty cycle of the LED is 0.3%.

A STIM300 initial measurement unit (Safran Sensing Technologies Norway AS, 2023) is mounted next to the motor to record the acceleration forces on the test stand. It has a range of 100 m/s^2 or ca 10 g per axis and is used at a sample rate of 2000 Hz. This is used to measure the vibrations to asses the forces during ice shedding events.

The calibration of the dynamometer has been checked for the temperatures −2 °C, −5 °C, −10 °C, −15 °C, and −20 °C, using a 1 kg weight on a 20 cm offset of the axis of the motor. The measured torque value is then compared to the expected value. These values can be seen in Table 1. From these measurements, a correction factor has been calculated to compensate for the reduction in the measurement torque due to the low temperatures. Before each run, the force measurements are set to

zero to ensure that the measurements are not influenced by any drift during the previous runs.

A challenge for the measurement of the thrust and torque of the propeller is the vibrations created by ice shedding off the propeller. The ice shedding can be asymmetrical. An imbalance between the ice on the propeller blades can lead to high-vibration events that can occasionally lead to a persistent measurement error after the ice shedding event. In one run, the ice shedding has led to unrealistically high efficiency, which has been thus handled as an exception and excluded.

For the analysis of the performance of the IPS, the efficiency η_{clean} of the propeller was analysed. For this calculation, the thrust T_{clean} and torque Q_{clean} of the clean configuration were used to calculate the efficiency of the clean configuration with respect to the air velocity v and the rotation rate n. This led to the following equation:

$$\eta_{\text{clean}} = \frac{T_{\text{clean}} \cdot v}{Q_{\text{clean}} \cdot 2 \cdot \pi \cdot n}, \tag{1}$$

with an identical air velocity and rotation rate between the iced and the clean experiment, the efficiency η_{rel} relative to the clean efficiency can be calculated as follows:

$$\eta_{\text{rel}} = \frac{T_{\text{iced}}/T_{\text{clean}}}{Q_{\text{iced}}/Q_{\text{clean}}}. \tag{2}$$

The thrust vector is assumed as pointing in the direction of the travel of the UAV, so that in the case that the propeller creates a force in the opposite direction, the thrust T_{iced} and the relative efficiency η_{rel} will have negative values. To enable the comparison of different runs, a time average of the efficiency of the propeller is calculated. The forces are averaged from 60 s of ice accretion until the end of the run when the spray system is switched off. The first minute is excluded to remove the initial ice accretion from the averaging. In most runs up to −10 °C, this will be after the first ice shedding event. At −15 °C the performance after 60 s has degraded below the peak performance reached after an ice shedding event. Thus the averaging after 60 s will allow for a comparison of the long-term performance between different runs.

The icing conditions were chosen to cover the typical flight conditions of fixed-wing UAVs. The airspeed is 25 m/s, and the rotation rate of the propeller of 4200 rpm.

The tests were started by activating the airflow in the wind tunnel. At the same time, the motor turning the propeller was started. Both systems were given 30 s to stabilise. Then the spray system of the wind tunnel was switched on to simulate the cloud. At the same time, the power to the IPS was started. The experiments were repeated multiple times at different power levels. The testing duration was 240 s for the ice accretion experiments to be used as a baseline. Tests with an activated IPS were performed at −5 °C and −10 °C for 180 s at different power levels to see the influence of different power levels on the performance of the propeller. Long-term tests with 600 s of ice accretion and IPS run time were performed at −10 °C and −15 °C. This was done to get data on the performance of the IPS during extended icing conditions. An overview of all the experiments performed is given in Table 2 and a detailed list of all runs can be found inTable A4. The IWT run number references the run number used during the experimental campaign, with the suffix IWT-2 or IWT-3 naming the specific experimental campaign in which the results were calculated. The error margins have been taken from previous measurement campaigns in the IWT by Hann et al. (2021) and Jokela et al. (2019).

2.3. Numerical analysis

To assist in the design of the propeller IPS, the tool ANSYS FENSAP-ICE version 2022R2 was used to analyse the heat fluxes on the propeller. The numerical setup was based on a previous work analysing the ice accretion on the same propeller as used in this work (Müller et al., 2021).
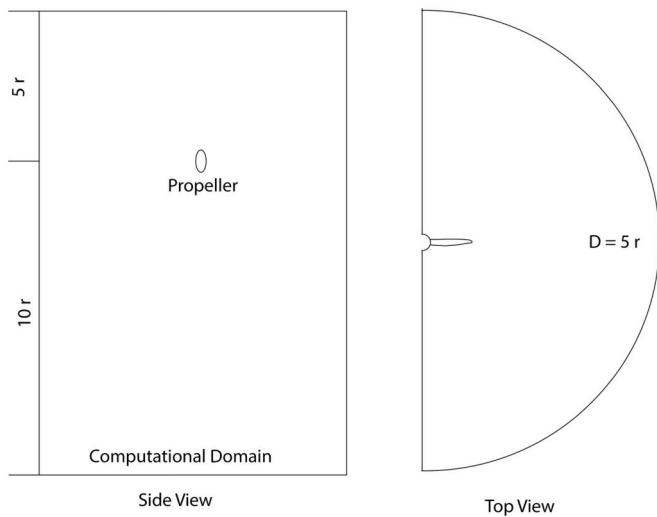
Fig. 4. Computational domain used for the numerical propeller simulations.

ANSYS FENSAP-ICE is an icing CFD code for calculating in-flight icing (Beaugendre et al., 2005) that has been used on UAVs (Tran et al., 2004; Hann et al., 2020). FENSAP-ICE consists of three different modules used to calculate the airflow, the droplet distribution and finally, the ice accretion and anti-icing heat loads. FENSAP is the flow solver used, a finite element flow solver using the Reynolds averaged Navier–Stokes equations (Baruzzi et al., 1995). The impingement of the droplets onto the propeller has been calculated using the module DROP3D included in ANSYS FENSAP-ICE (Bourgault et al., 2000). It uses an Eulerian approach to calculate the droplet distribution (Bourgault et al., 1999). The required anti-icing loads have been calculated using the module ICE3D (Bourgault et al., 1999; Beaugendre et al., 2003), which uses the Messinger approach to calculate the energy equations on the surface of the propeller (Messinger, 1953).

The geometry of the propeller has been provided by Mejzlik Propellers. A single propeller blade was simulated in a 3D simulation with the rotation represented using a moving reference frame, and the second propeller blade was included using a periodic interface. A 3D model of the spinner used in the experiment is included in the geometry. The computational domain can be seen in Fig. 4. In the simulation setup, a half-cylinder was used to create the mesh. The simulation domain has a diameter of 5 times the propeller radius. It has an extent of 5 times the radius towards the front and 10 times the radius towards the rear of the propeller. The computational domain is created with Cadence Pointwise version V18.6R2 (Cadence Design Systems, Inc., 2023), and the mesh is

created with ANSYS Fluent Meshing. The mesh uses a hybrid grid with 37 prism layers. The height of the first prism layer is 50×10^{-5} m to ensure a y-plus value smaller than one over the entire airfoil surface. The final mesh has 10×10^{6} cells. The mesh used is shown in Fig. 5. A mesh convergence study on the geometry has been performed by Müller and Hann (2023).

A fully turbulent Spalart–Allmaras turbulence model has been used to calculate the airflow of the propeller. The surface roughness was set to 0.0005 m. There are two options for calculating the heat loads of the propeller required to keep the propeller ice-free. The running-wet mode calculates the heat load to keep the surface of the propeller at 0 °C without any ice accretion and the fully evaporative evapoates the impinging fluid(Hann et al., 2021). The running-wet heat fluxes on the propeller were analysed to design the IPS, as this operational mode leads to lower overall power requirements compared to a fully evaporative design. Furthermore, the maximum temperature limits of the resin would prevent the operation in a fully evaporative mode. Three cases were selected to analyse the required anti-icing heat fluxes. They were chosen to correspond to the conditions tested at the icing wind tunnel. One was used at a temperature of −5 °C, representing a typical glaze ice shape on the propeller, at −10 °C representing a mixed ice shape, and one at a temperature of −15 °C to represent a rime ice shape. This heat flux distribution could then be used to choose an appropriate layout for the IPS.

The calculated heat flux distribution was then used to estimate the IPS power requirements for the system. These values could later be compared to the power drawn by the IPS during the experiment to get a comparison between the numerical and experimental consumption levels. The comparison can then be used to start the process of validation of the numerical results.

The required power for the IPS has been calculated with a method based on the peak heat fluxes on chordwise sections of the propeller. In this method, the required heat flux of each zone is analysed and then combined to get the IPS power for the anti-icing of the entire propeller. Previous work has shown that ANSYS FENSAP-ICE can estimate the IPS loads on the wings of UAVs (Hann, 2020). That work compared the specific heat fluxes from the simulations with the experimental data and detected that the predicted running wet peak heat flux from ANSYS FENSAP-ICE corresponds well to the required running-wet anti-icing heat fluxes in the experiment. In the same work, the required heat fluxes on the propeller were estimated based on numerical data. To apply the latter method to the propeller, it had to be adapted to work with the changing spanwise heat fluxes and the use of two spanwise heater zones with fixed heat flux ratios. To solve the issue of spanwise variations, the required peak heat flux was calculated for both zones separately. The higher value was used to calculate the required power of the entire propeller based on the known ratio of heat flux between the zones. If the
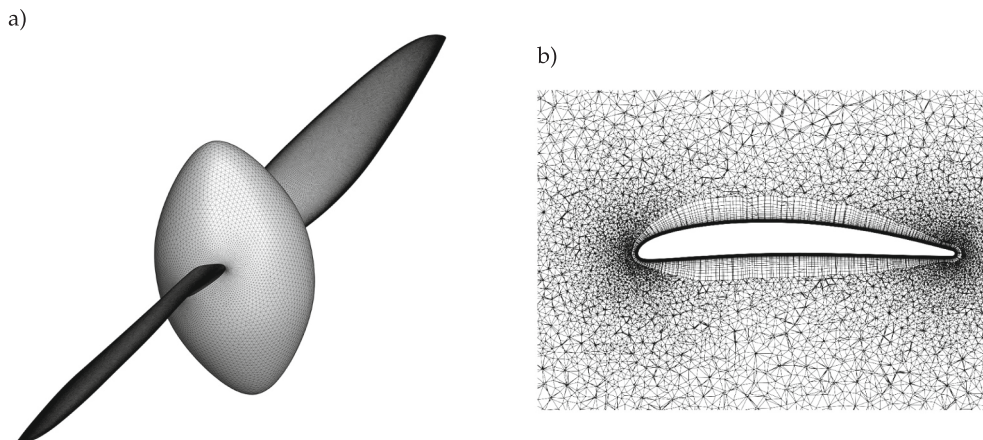

Fig. 5. Mesh of the propeller a) on the surface of the propeller, and b) on a section at 80% of the radius.
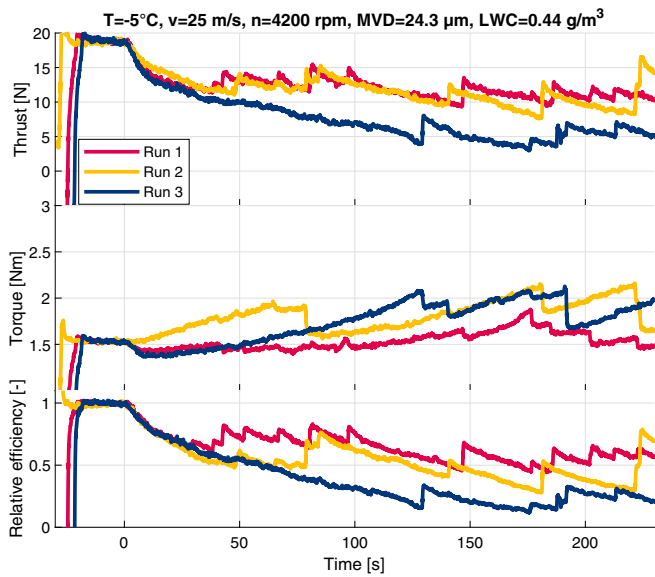
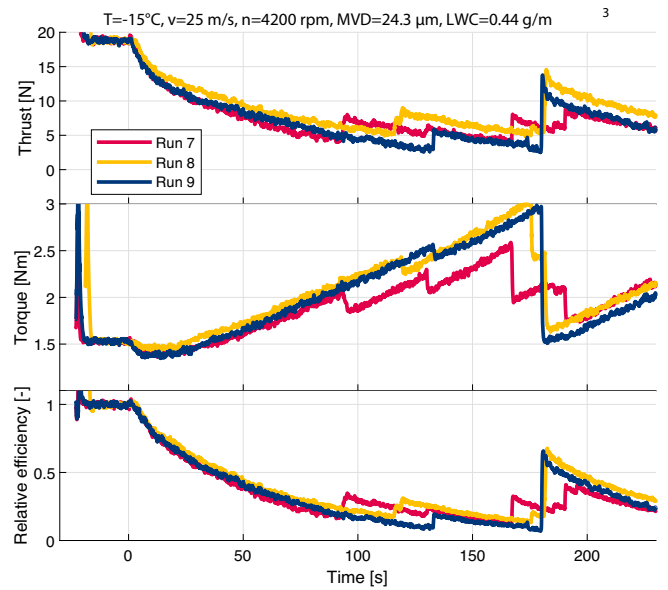**Fig. 6.** Propeller performance degradation without IPS for −5 °C.

Fig. 8. Propeller performance degradation without IPS for −15 °C.

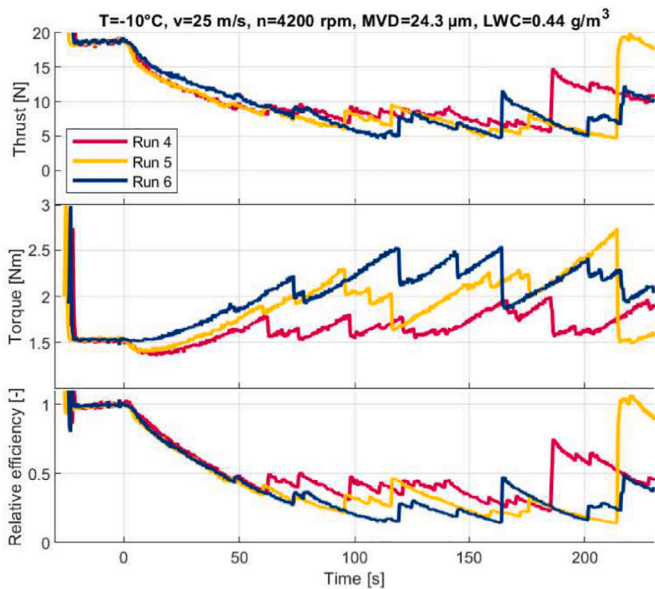**Fig. 7.** Propeller performance degradation without IPS for −10 °C.

peak heat flux in the root section is so high that the outer section would provide more than the predicted required heat flux, the heat flux in the root zone would be used to calculate the total heat flux and vice versa. The total power input to the propeller P_{IPS} was then calculated from the length l and width w of the root and tip zones, as well as the calculated required heat fluxes q_{root} and q_{tip} where q_{tip} equals two times q_{root}. This leads to the following equation:

$$P_{IPS} = l_{root} \cdot w \cdot q_{root} + l_{tip} \cdot w \cdot q_{tip},\tag{3}$$

which can be used to calculate the required power of the propeller IPS.

3. Results

First, the experimental results of the unheated propeller experiments are presented, showing the performance degradation of the propeller in icing conditions. Then the numerical analysis results of the anti-icing heat fluxes are shown. At last, the experimental results for the heated

propeller are presented.

3.1. Experimental results

First, tests without IPS were performed to establish a baseline for each temperature. These tests were performed at the conditions shown in Table A4. The test duration was 240 s. The results are shown in Fig. 6. In this figure, the thrust, torque, and relative efficiency η_{rel} are plotted over the ice accretion time. The time 0 is set as the time at which the spray system of the IWT is activated, i.e., the time from which ice accretion begins. In these experiments, the propeller experienced a rapid loss of thrust and an increase in torque. The gradient of the initial performance degradation between 0 and 45 s is similar between all three runs. After the initial degradation, a critical point is reached at which the amount of accumulated ice on the blade becomes so large that the centrifugal forces overcome the ice adhesion forces. This leads to the fracturing of the ice and, consequently, ice shedding from the propeller. The sudden loss of ice leads to a change in aerodynamics and, thus, a sudden recovery of the propeller efficiency. These ice shedding events typically occur asymmetrically, only on one blade. The resulting imbalance between the prop blades leads to high vibrations, which typically only stop when the opposite blade sheds ice. With the ice shedding, larger differences between the runs are visible. For runs 1 and 2, the first ice shedding occurred before 50 s, while in run 3, the ice only shed after 120 s. The long-term average efficiency between 60 and 180 s shows variations between runs, with one run at around 61% of the clean performance, one at 49%, and one at 27%. The ice appeared as a mixed ice shape with translucent ice on the leading edge, and two ice horns.

For the baseline case at −10 °C, as shown in Fig. 7, the variation during the ice shedding is not as large compared to the −5 °C case. Again, the initial performance degradation is similar between the three runs until the first ice shedding event, which occurs later than at −5 °C. All three runs show the first ice shedding event between 60 s and 75 s. The time-averaged efficiency after ice shedding is lower than the efficiency at −5 °C. The gradient of the initial performance degradation is steeper than at −5 °C. The variations in the time-averaged efficiency after more than a minute of icing are lower, ranging from 26% to 41%. The ice shape was still mixed, with ice horns which are not as pronounced as at −5 °C.

For the case at −15 °C, shown in Fig. 8, the first ice shedding event is once again occurring later, with the first ice shedding events happening between 90 s and 135 s. The propeller performance drops lower than at
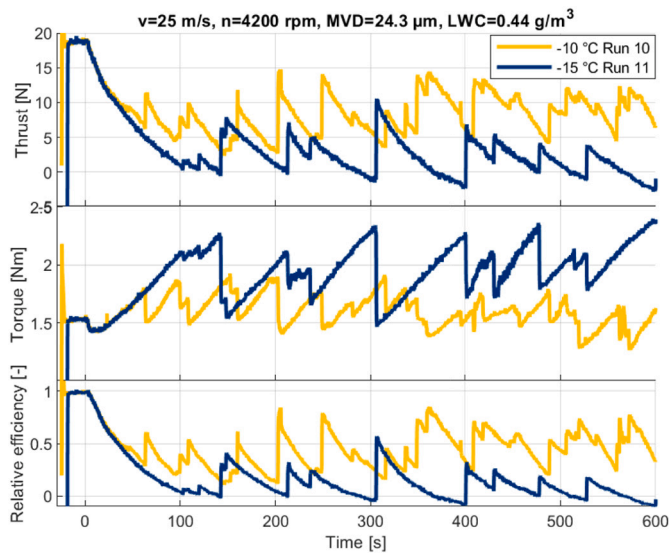
Fig. 9. Icing performance degradation without IPS for −10 °C and −15 °C during 600 s ice accretion experiments.
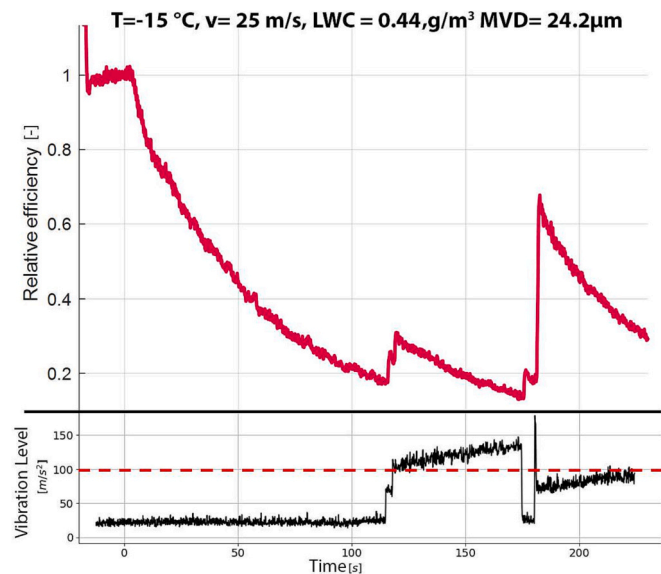

Fig. 10. Level of the vibration at the motor. The dashed red line represents the saturation level of the accelerator.

Fig. 11. Running-wet anti-icing heat flux on the propeller at a temperature of −15 °C. The black borders represent the extent of the heating element used in the design.

Fig. 12. Peak running-wet heat flux on the propeller on multiple chordwise sections along the radius of the propeller.

−10 °C and −5 °C. The intensity of an ice shedding event can be estimated from the amount of performance the propeller is able to recover. With this metric, the first run at −10 °C shows the strongest ice shedding event, followed by the strongest ice shedding events at −15 °C. This is important, as ice shedding events will induce strong vibrations into the system. At this temperature, the ice represented a streamwise rime ice shape.

The results of the two long baseline runs can be seen in Fig. 9. Those runs show a similar behaviour as the shorter experiments. For the run at −10 °C, the run shows that the periodic ice accretion and ice shedding behaviour will continue. This periodic behaviour was not observable with the short ice accretion time of 240 s at −15 °C, as the time between ice shedding events is longer for the colder temperatures. At −15 °C, a significant ice shedding event occurs roughly every 100 s, while at −10 °C, they occur about twice as often. The thrust of the propeller is showing negative values. This is caused by extensive ice shapes which lead to the thrust vector pointing in the same direction as the airflow.
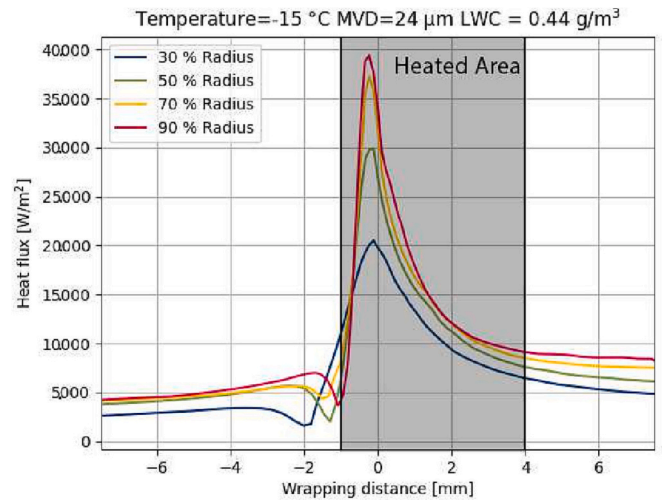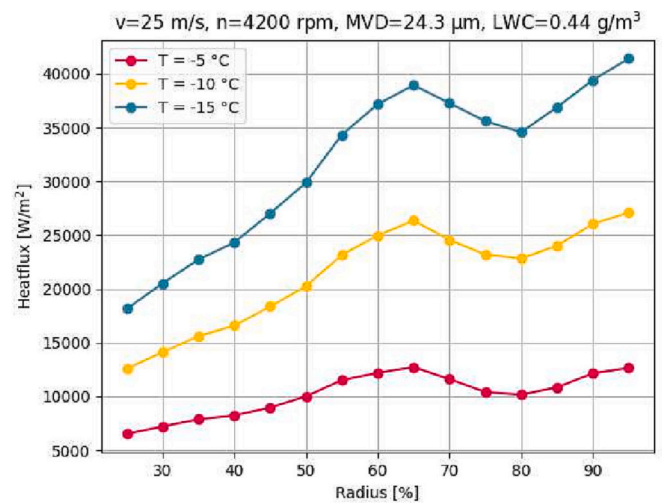
This negative thrust value is also leading to a negative relative efficiency if the negative thrust is inserted in Eq. (2).

To highlight the impact of the ice shedding on the vibration level, the vibration level for one run at −15 °C was plotted over the measured performance degradation. This is shown in Fig. 10. The first ice shedding event creates a condition in which the propeller is experiencing sustained high levels of measured vibrations. These vibration levels are above the saturation level of the acceleration sensor at 100 m/s^2 for a single direction. Therefore, the actual level could be higher than measured. This lasts until the next ice shedding event at 170 s. This restores the vibration level to the baseline for a short moment, before the next ice shedding event is recorded. Shortly after this, a strong ice shedding event is recorded. The measured level of 175 m/s^2 indicates that the sensor has reached its saturation level in all three axes simultaneously. Following this event, the vibrations stay at a constant high level but below the saturation level of the sensor.

3.2. Numerical heat load results

The numerical heat loads have been simulated with FENSAP-ICE. The chordwise heat flux distribution for multiple spanwise locations
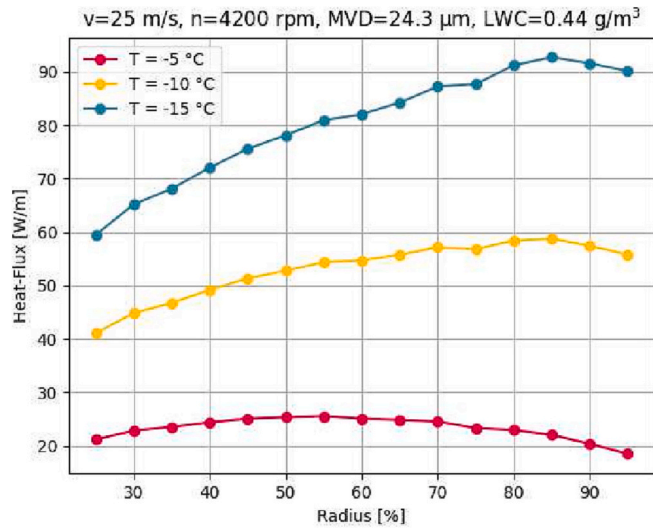
Fig. 13. Total heat flux integrated over the surface of heating element in multiple chordwise sections.

Table 3

Results of the numerical analysis of the heat fluxes on the propeller over the propeller and the heating element.

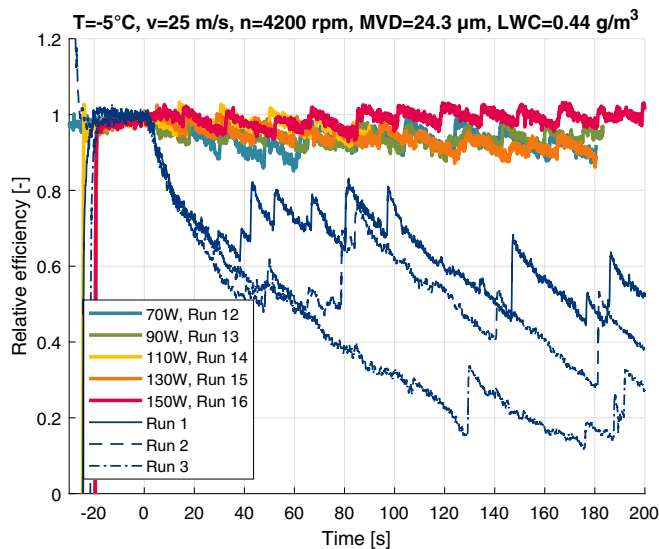| Temperature	Estimated IPS power
−5 °C	46.2 W
−10 °C	97.0 W
−15 °C	138.6 W

Fig. 14. Change in efficiency of the heated propeller at −5 °C, compared to the unheated propeller.

was calculated for the conditions used in the experiment. In Fig. 11, the required running-wet heat fluxes are plotted over four chordwise sections of the propeller. The position is plotted as the wrapping distance, which is the distance along the surface of the propeller from the leading edge. The distances are normalised with the chord length of the propeller at each section. Positive values signify the suction side of the propeller, while negative values indicate the pressure side of the propeller. The figure shows that the peak heat flux is moving a small amount further towards the lower surface the further outwards on the propeller they are. It also shows a steep decrease in the required heat
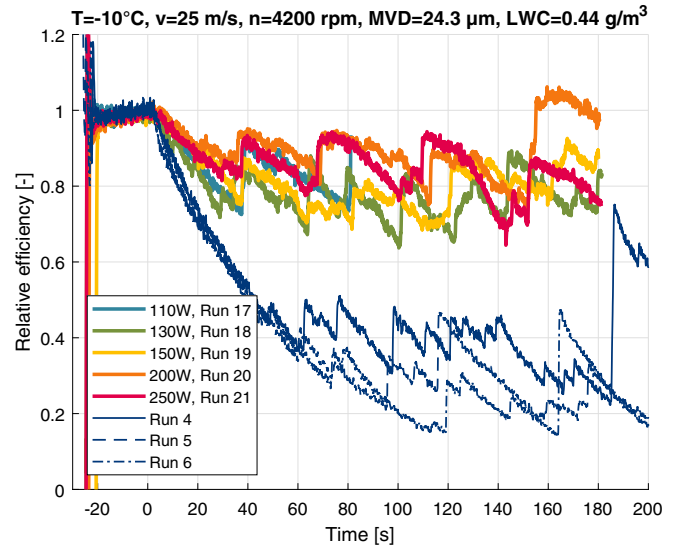

Fig. 15. Change in the efficiency of the heated propeller at −10 °C, compared to the unheated propeller.

flux on the lower surface, while the heat flux on the top surface decreases more gradually.

The chordwise peak heat flux over the different temperatures is shown in Fig. 12. The peak heat flux increases with the radius for all three temperatures. The colder temperatures show a higher required running-wet heat flux compared to the higher temperatures. At 70% of the radius, the linear increase of the peak heat flux of the propeller drops until the trend is re-established at 80%.

In Fig. 13, the running wet anti-icing heat flux is shown for each section integrated over the area of the heating element. This shows a near-linear increase of the required anti-icing heat flux with the radius for −15 °C. The gradient for −10 °C is not as steep as the gradient at −15 °C, and at −5 °C, the required heat flux at the tip is not as large as the heat-flux in the middle, with a slight increase in the center.

To analyse the required anti-icing power for the propeller IPS, the required heat fluxes were calculated as described in Chapter 2.2. In all conditions, the heat flux is calculated based on the peak heat flux in the root zone at its outermost point of 50% of the radius. The results of this calculation are shown in Table 3. The predicted IPS loads increase roughly linearly with the temperature.

3.3. Heated propeller results

In this section, the results from the heated propeller tests are presented. The propeller ran with five different levels of supplied power at −5 °C. Here the IPS power was varied from 70 W to 150 W, corresponding to a heat flux on the root zone of 15 kW/m² to 32 kW/m² and on the tip zone of 30 kW/m² to 65 kW/m². The resulting propeller efficiency can be seen in Fig. 14. In this plot, the relative efficiency η_{rel} of the propeller is shown over the ice accretion time. The ice accretion runs for the propeller without an IPS are shown as a baseline. The thrust and torque values are not shown to increase the readability of the plots. In contrast to the steep performance degradation in the performance of the propeller, the heated propeller runs show a very low reduction of the relative efficiency. After about 40 s, the first unheated propeller run shows a sudden recovery of the relative efficiency, which is likely caused by an ice shedding event. In general ice shedding occurs earlier and at less intensity, starting at 15 s. Furthermore, the spread in efficiency is smaller than for the unheated propeller. After 60 s of icing, the unheated propeller shows variations in the relative efficiency from 15% of the original value to 82% of the original value. Compared to this, no IPS propeller run drops below 85% of the efficiency of the clean propeller.
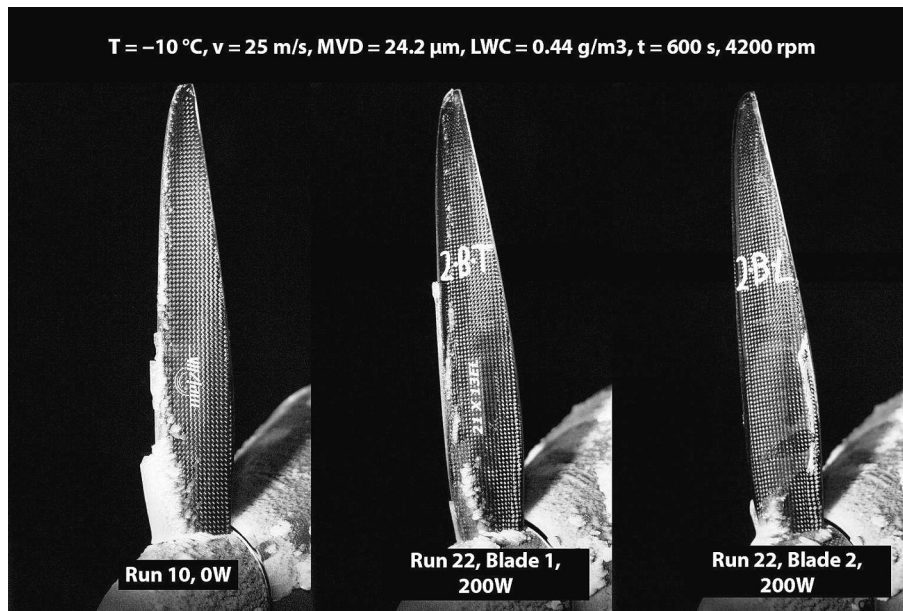
Fig. 16. High-speed camera images of the IPS propeller in icing conditions at −10 °C after 600 s of icing conditions with 200 W heating power. Blade 1 shows residual ice after shedding, while blade 2 is clean.
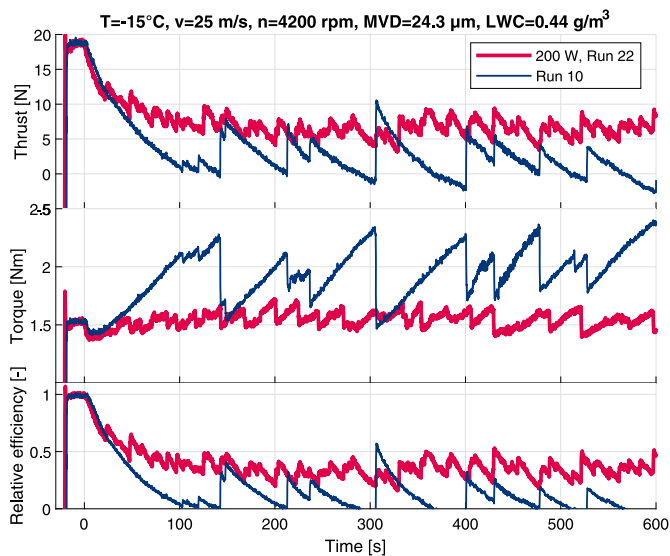
Fig. 17. Recorded thrust, torque, and the efficiency of the heated propeller at −15 °C, during a 10 min ice accretion test.

The run with the highest power input of 150 W shows the least degradation, but the run at 130 W shows the worst degradation. Thus there exists a variability between the experiments. It can be seen that even the run at 150 W still shows small losses in performance, followed by a sudden recovery of this, leading to the assumption that full anti-icing has not been achieved yet. Still, some ice is accumulating on the propeller. The results show that the time-averaged efficiency of the heated propellers is between 93% and 99% of the clean efficiency. The images from the high-speed camera are shown in Appendix B and show no ice accretion on the propellers in all the IPS runs.

For the experiments at −10 °C, the same analysis has been performed. For those conditions, the input power to the IPS was varied from 110 W to 250 W, corresponding to a heat flux on the root zone of 23 kW/m^2 to 54 kW/m^2 and on the tip zone of 48 kW/m^2 to 108 kW/m^2. The result of those runs is plotted in Fig. 15. The efficiency curve shows a significant gradient compared to the runs at −5 °C, but a lower gradient

than the unheated baseline. In contrast to the experiments at higher atmospheric temperatures, the heated propellers, in this case, are not able to recover the performance back to the performance of the clean propeller after ice shedding. This indicates that ice shedding is not removing all of the ice on the propeller. The data shows that the decrease in propeller efficiency due to the initial ice accumulation is reduced if the IPS power to the propeller is increased. The long-term efficiency is not significantly influenced by the power usage of the IPS, with all propellers changing between 65% and 95% of the clean performance with time-averaged values of between 79% and 89% for −5 °C and −10 °C respectively. While all IPS tests still show ice shedding, the variations in efficiency in baseline run 4 at 190 s and run 6 at 170 s are larger than the performance recoveries of the IPS propeller, indicating a reduction of the maximum mass of ice that is shedding of the propeller.

For a better estimation of the long-term performance, a 600 s IPS test was performed at 200 W. The heat flux at this power level is 43 kW/m^2 in the central area and 86 kW/m^2 in the outer zone. The results are shown in Fig. A21. This experiment showed the same cyclic behavior of ice accretion and ice shedding events as outlined in the 180 s tests. In Fig. 16, high-speed images of the IPS propeller and the unprotected propeller are shown. The unprotected propeller in run 10 shows ice accretion on the entire propeller. In the centre, the ice thickness on the leading edge is the largest, and then in three steps, the ice thickness on the leading edge is reduced for the protected propeller. Blade 1 shows a small amount of ice accretion in the centre and roughly in the middle of the propeller. The sharp edge towards the outside indicated that the ice had shed at that point. The propeller blade 2 shows no ice accumulation on the leading edge, except for a short area at the very centre of the propeller. From the centre of the propeller to the middle of the propeller, some runback icing on the trailing edge of the propeller can be observed.

The long-term ice accretion test was also reproduced at −15 °C, for which the thrust torque and relative efficiency η_{rel} are shown in Fig. 17. In this case, the initial gradient in the relative efficiency is the same between the heated and the unheated run. This indicates that at this temperature, the heater is no longer able to heat the surface of the propeller above the freezing point and to have any influence on the ice accretion. Only when the heated propeller starts to shed ice after 30 s do the efficiency curves move apart. Overall, the propeller performance is still degrading until it hits a stable periodic ice shedding and ice accretion cycle after 150 s. The time-averaged efficiency of the propeller
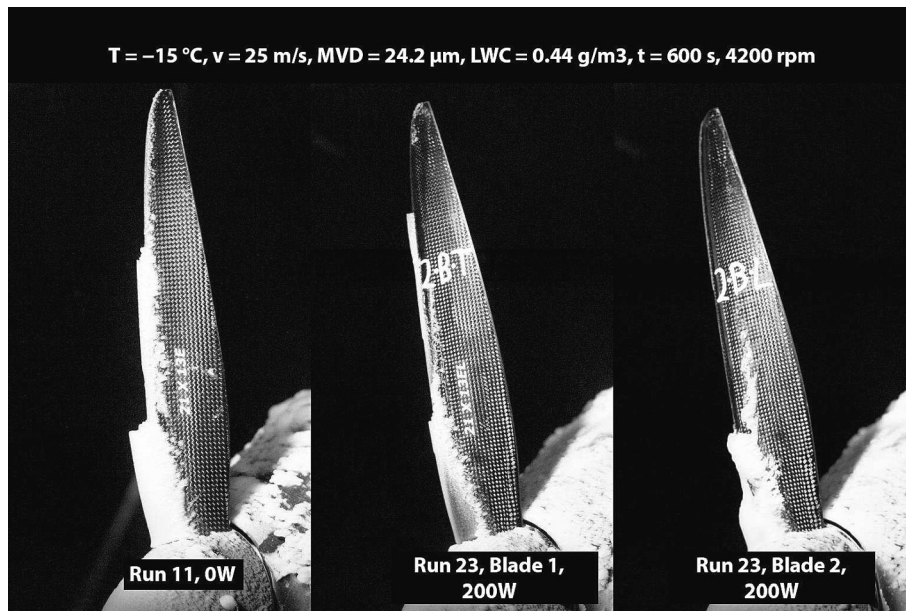
Fig. 18. High-speed camera images of the IPS propeller in icing conditions at −15 °C after 600 s of icing conditions with a heating power of 200 W. On blade 1 ice is visible on the leading edge, and on blade 2, some runback ice can be seen close to the trailing edge of the propeller.
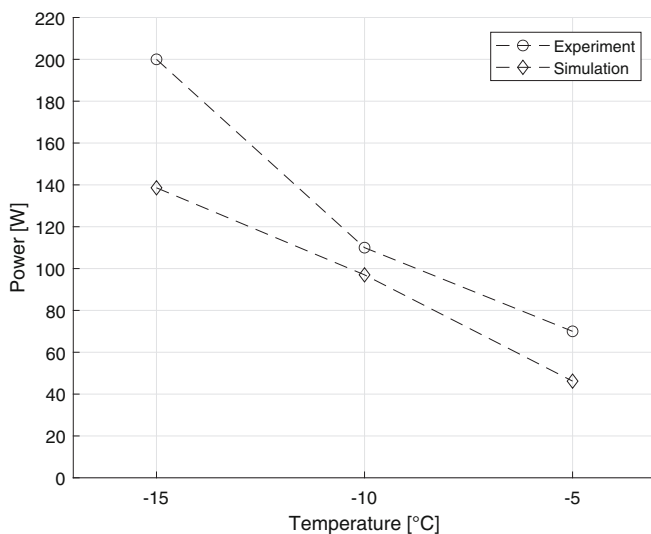

Fig. 19. Comparison of the simulated IPS power requirement with the used IPS power in the experiments.

after more than a minute of icing is 35%. The same is visible with the unheated propeller, which reduces its efficiency to 10% of its clean value on average. For periods, the relative efficiency of the unheated propeller is showing negative values, caused by the fact that the thrust of the propeller is now pointing in the opposite direction as before. Again the unheated propeller displays more frequent ice shedding events, but the variations in relative efficiency are smaller than for the unheated propeller. The comparison between the measured thrust and torque shows that the heating of the propeller is able to reduce the torque increase, however, the thrust remains reduced compared to the clean conditions, even when using the IPS.

In Fig. 18, high-speed images of the IPS propeller and the unprotected propeller are shown at the end of the run after 600 s of icing conditions. The unprotected propeller in run 11 shows ice accretion on the entire propeller. Compared to the ice accretion at −10 °C in Fig. 16, the ice thickness in the middle of the propeller is higher. Blade 1 of the protected propeller shows significant ice accretion in the centre of the

propeller, with some ice accumulation towards the middle. The tip region is comparatively ice-free. Blade 2 shows some ice accumulation in the centre of the propeller, but from the middle outwards, the leading edge of the propeller is ice-free. In the middle of the propeller, some runback icing can be observed at 40% of the chord of the propeller. The ice accretion on the centre of the propeller is connected to the spinner, indicating that the spinner might be responsible for the missing ice shedding on the centre of the propeller. Still, the ice accumulation along the leading edge of the propeller indicates that the heat fluxes are insufficient to achieve anti-icing. Additionally, ice is accumulating on the spinner itself, which could lead to an increase in the torque measured.

4. Discussion

In this section, the uncertainties associated with testing at an IWT are examined; additionally, the ice accretion results are discussed, followed by the heated propeller results and the numerical results. Lastly, the results are compared to other works in the literature.

4.1. Ice accretion experiments

The experimental method of analysing the forces on the propeller enables a detailed look at the performance of the propeller during the icing condition. The largest challenge of the testing is related to the vibrations created by the imbalance of forces due to ice shedding events. Asymmetrical ice shedding between propeller blades can cause an imbalance between the mass of the propeller blades and the aerodynamic forces acting on each of the blades. This causes vibrations. A short overload of the load cell can lead to sudden offsets in the measurements of the forces by the dynamometer. Offsets happen randomly and are, therefore, difficult to correct. To limit the impact of this effect, thin silicon-coated wires have been used to connect the IPS power transfer unit and the motor. This reduces the forces those wires can act on the force sensor due to their stiffness and which could fluctuate if the position of the wires moved due to strong vibrations. Another possible error source is ice accumulation on the force sensor and the motor. To avoid this ice accretion, a protective aerodynamic cover was placed in front of the force sensor to prevent ice accretion on the force sensor. After each run, it was checked if ice bridges had developed between

parts before and after the force sensor. With these precautions, the dynamometer is expected to measure the forces on the propeller, especially in the first part of the ice accretion. After ice shedding events, the measured forces might experience some offset, but the qualitative trend will still be captured. This will allow for the evaluation of the anti-ice ability of the propeller IPS system. These vibrations measured with more than 100 m/s^2 or ca. 10 g per axis could lead to mechanical damage in the motor and the UAVs. Due to the strong vibrations, controlling or preventing strong ice shedding events is an important factor in enabling the operation of UAVs in icing conditions.

Another source of uncertainty is the inhomogeneous LWC distribution across the wind tunnel. The LWC will not be constant across the entire area of the wind tunnel (Hann et al., 2023). This difference is due to wall effects inside the wind tunnel as well as gravity effects on the droplets. The LWC will not be constant between the centre and the outside of the propeller as they are in different parts of the wind tunnel. The calibration of the LWC in the IWT is performed on the centre of the wind tunnel, and experiments measuring the LWC distribution in the IWT have shown that the tip of the propeller will receive less water than the centre (Hann et al., 2023). A second influence is the unevenness of the velocity of the airflow. This is caused by the blockage of the wind tunnel by the propeller (Fitzgerald, 2007) and the wall effects of the wind tunnel (Garner et al., 1966). It is expected to have a maximum at the centre and lower values towards the tip of the propeller. This effect leads to elevated ice accretion rates near the centre compared to the tip. Also, the aerodynamic forces along the propeller will be affected, with a relative increase in the angle of attack toward the outside of the propeller, compared to ideal inflow conditions.

Another effect is that the propeller accelerates the airflow and thus will increase the inflow air velocity compared to the IWT freestream air speed validation without a propeller mounted. In contrast to the blockage of the propeller, the dynamometer will block some of the air flow in the wind tunnel. The blockage caused by the dynamometer will lead to an increase in the flow velocity toward the outside of the propeller. This will influence the performance measurement of the propeller by reducing the measured thrust, but the effect is expected to be constant during the run if the conditions of the propeller are constant. As the aim of the IPS is to prevent ice accretion and thus keep the performance of the propeller constant, the measurements can still be used to evaluate the performance of the IPS system. The flow conditions will influence the degree of performance degradation, but as the influences are similar for all tests, it is expected that the relative trends will be maintained.

The unheated propeller showed a strong decrease in propeller performance during icing conditions. This performance reduction is dependent on the temperature. With lower temperatures, the thrust is reduced more compared to higher temperatures. This is explained by the longer ice accretion time until the ice starts to shed off the propeller. Ice shedding occurs earlier at higher temperatures and later at colder temperatures. A reason for this is the change in ice adhesion forces at higher temperatures (Makkonen, 2012). This ice shedding can lead to large variations in the performance of the propeller between runs with the same conditions if the ice shedding event is happening at different times. In experiments performed directly after each other on the same equipment and propellers, the ice shedding proved to vary significantly between the runs, leading to problems in quantifying the results of the experiment as the results have to be averaged over a longer time period and multiple runs. A possible reason is the inherent stochastic behaviour involved in icing (Hann, 2019). Another possible cause for the differences could be surface contamination, as could be introduced in cleaning the propeller between runs. These would change the adhesion characteristics between the propeller and the ice. The propeller was cleaned with a paper towel between runs to avoid contamination. A potential cause for contamination occurs during the propeller cleaning process, where oils could be transferred to the propeller. The influence of contamination of the propeller will influence the measurements of the performance in single runs, to counteract this most experiments have

been performed repeatedly to minimise the influence of random events.

4.2. Heated propeller experiments

Over the tested temperature range, the IPS has shown multiple behaviours in relation to its anti-icing ability. For the highest temperatures of −5 °C, the propeller has been able to keep the propeller in a mostly ice-free condition, with no permanent reduction in the efficiency of the propeller. Small amounts of ice have been observed to accumulate on the propeller and to shed, although, after each shedding event, the efficiency of the clean propeller is mostly restored. For the temperature at −10 °C, the IPS was not able anymore to retain the clean performance of the propeller but was able to stabilise the efficiency of the propeller at a time-averaged value of 65% of the clean propeller efficiency, compared to the time-averaged value of 43% for the unheated propeller. This means that the IPS propeller is able to retain 20% more performance.

In the IPS run at −10 °C, after each ice shedding event, not all ice on the propeller has been removed, and the remaining ice has a negative effect on the performance of the propeller. An increase in power has no significant effect on the time average relative efficiency. Some ice remains outside the protected area, as can be seen in the high-speed images. Thus an increase in the power of the IPS does not affect the accumulated ice in those areas. Additionally, the IPS power is insufficient for effective anti-icing, leading to ice accretion in the protected areas. Ice accumulation outside of the protected areas might be caused by runback water from the protected zones or impingement in areas not protected by the IPS. This suggests that an extension of the protected areas may be required to reduce this effect. Uneven IPS loads between the propeller blades could affect the de-icing performance of the blade with less heat flux.

This effect is even stronger at −15 °C. Here the time-averaged efficiency drops to 35% of the clean value, compared to a time-averaged value of 10% for the unheated propeller. The unheated propeller experienced phases of negative thrust, but with the IPS, the ability of the propeller to create thrust has been preserved. Ice-shedding events occur much more frequently and with less impact on the efficiency of the propeller compared to the unheated propeller. This would likely reduce the strength of the vibrations created by uneven ice shedding and the danger of ice fragments breaking off the propeller. While the IPS is not operated in a periodic cycle like a de-icing system, the cyclic ice shedding leads to similar cyclic behavior. This highlights the fact that an IPS can be a useful tool to enable the UAV to be flown in icing conditions, even if the total used heating power is lower than the required heat flux.

4.3. Numerical heat load results

The numerical analysis of the IPS has been used as a tool for the practical implementation of the IPS. The difference in the trends of the peak and integrated anti-icing loads in Figs. 12 and 13 highlights the challenges with the use of zones, which have fixed heat flux ratios. When the temperature is varied, the ratio between the two zones is also changing. One cause for this is the variation in stagnation temperature over the radius of the propeller, as the areas with higher air velocities will see higher adiabatic heating as the Mach number increases. Likely, variations in the rotation rate, the LWC of the air and the flight velocity will also influence the ideal heat flux distribution. For this reason, having fixed ratios between the spanwise zones might lead to a reduced performance of the system. In this design, the chosen heat flux ratio of two between the zones is too high based on the numerical results. In all simulations, the predicted peak heat flux in the center zone is higher than twice the heat flux in the outer zone. This deviation from the predicted ratio will lead to reduced efficiency of the propeller as the outer part of the propeller will receive more heat flux than required for successful anti-icing.

In Fig. 19, the predicted heat fluxes from the simulation are compared to the heat fluxes in the experiments. For the experiments at

−5 °C, −10 °C and at −15 °C, the lowest used power of 70 W, 110 W and 200 W respectively is shown, as there was no significant difference observed between the experiments at different power levels. It is important to note that for −10 °C, the propeller was not able to achieve full anti-icing, with ice accumulating on the propeller, indicated by the ice accretion observed on the leading edge of the propeller. Even an increase of the IPS power to up to 250 W was not able to recover the performance. The same is true for the case at −15 °C, which was not able to achieve full anti-icing but only recovered parts of the performance of the propeller.

The numerical data underestimates the required heat fluxes for anti-icing. This could be due to several factors internal to the simulation or with the experiments. The difference could be caused by the heat conduction inside the propeller. There are two layers of carbon fibre between the heating element and the outside, which could spread the heat flux over a larger area than the heating element has. Furthermore, any imbalance between the resistance of the heating elements on both propeller blades will lead to an imbalance in the power output between both blades. Full anti-icing is only achieved when both blades are ice-free, which would also increase the required heat flux over the predicted amount.

The use of the peak heat flux for the estimation of the required heat flux on the entire heating element enables a good estimation of the required heat flux in this setup based on the comparison with the experimental heat loads. The simulations of the required heat flux have shown that the peak heat flux in Fig. 12 is not showing the linear increase with the radius of the integrated heat flux over the heating element is showing. The expectations of a linear increase in the peak heat flux would be based on the increasing air velocity relative to the propeller with the radius. This is due to variations in the airfoil of the propeller with a different leading edge radius. This might indicate the benefits of using surface-integrated heat fluxes over the heating element for the heater design. While the prediction of peak heat fluxes is very dependent on the specific geometry close to the stagnation point, the surface-averaged heat flux will have less impact as the value is averaged over a larger area. More work must be done on estimating the required heat flux over the surface of the heating element versus trying to produce the required peak heat flux.

A second source that can lead to differences between experiment and numerical results is the coarse mesh due to limitations of the available power. Therefore, the ability of the simulation to capture very narrow peaks in required heat flux is diminished, while the heat fluxes over a wider area might still be captured. Future optimizations might be using a finer mesh or 2D simulations that could afford to resolve the leading edge at a higher resolution. The advantage of the chosen approach is that the analysis is not limited to a few sections and that the 3D flow phenomena are resolved inside the simulation.

One further important factor for the differences between numerical and experimental results is the turbulence model, which could have a significant impact on the calculation of the heat flux. Higher-order turbulence models, which include the transition between laminar and turbulent boundary layers, might improve the prediction of the simulations. The difference is due to the lower heat transfer coefficient in a laminar boundary layer, which would reduce the anti-icing heat fluxes. Further challenges for the numerical prediction of the anti-icing heat fluxes are highlighted by Hann in Hann (2022) and include the surface roughness modeling, which has a large influence on the estimated heat fluxes and possible laminar separation bubbles. The methods used have been developed for use on the wings of manned aviation aircraft, and as such, the Reynolds number on the propeller is lower than the range the tools have been validated against.

Additional differences between the experimental and the numerical results could be found in the difference in the flow boundary conditions

caused by the open wind tunnel section compared to the used cylindrical computational domain used in the CFD simulation, which imposes the boundary conditions of a closed test section with a larger diameter. These challenges are caused by the lack of validation data that could be used to validate the numerical prediction of anti-icing heat fluxes on the propellers of UAVs. In the presented work, the method of analysing the peak heat fluxes on the heating element is shown, which could be used to predict the IPS power for a propeller. A full verification and validation of the method must be performed once more experimental data is available to get a broader experimental data set and verify the simulations.

4.4. Comparison to other work

Recently, multiple solutions to the issue of an IPS on rotors of UAVs have been published, focusing either on surface coatings (Liu et al., 2018; Han et al., 2022; Villeneuve et al., 2022) or electro-thermal systems (Karpen et al., 2022; Meteomatics, 2017; Hann et al., 2019; Wallisch and Hann, 2022). Most such systems target the rotors of smaller multi-rotor UAVs. Compared to those solutions, the design presented in this paper targets a propeller with a larger diameter, which creates more thrust. The increase in size leads to an increase in the power requirement and a higher required anti-icing heat flux. As the heating element is inside the structure, compared to IPS designs that use heating foils that are placed on the surface of the propeller, the presented solution should not affect the performance of the propeller outside of icing conditions, except for friction introduced by the slip ring. As the heating element in this study is manufactured out of the same material as the propeller, it could be part of the load-carrying structure of the propeller, reducing the added weight of the system. The disadvantage of the placement of a heating element inside the structure is a possible increase in the required heat flux to achieve anti-icing.

Compared to the work by Karpen et al. (2022), the IPS proposed in this study was able to keep the propeller ice-free at temperatures of −5 °C compared to the 0 °C. At lower temperatures of −10 °C and below, both systems were not able to prevent ice accumulations and created a pattern of regular ice shedding events. The solution for an IPS presented in this work might allow the UAV to be flown through continuous icing conditions because it is powered through a slip-ring and thus can be connected to the main power supply of the UAV. This is compared to solutions with a power source in the rotating part of the system, which is going to allow only short flights in icing conditions until the energy supply has been depleted. Such as system was developed by Karpen et al. (2022). The IPS, in their design, is meant to operate on a multirotor UAV for short-duration flights in adverse conditions. Therefore the time limit of the protection to 15 min is acceptable. The disadvantage of the presented solution is that the used slip ring will always introduce some friction and thus reduce the motor efficiency. Another disadvantage of the slip ring is the related maintenance.

The surface coatings developed in other works (Villeneuve et al., 2022; Liu et al., 2018; Han et al., 2022) show the potential to reduce the ice adhesion forces and to increase the ice shedding frequency. However, they were not able to keep the propeller ice-free at lower temperatures. This behavior is similar to the presented IPS in this paper. The advantage of the coating is that they do not rely on power during the operation. A disadvantage of the currently existing surface coatings is their low durability, which limits their effective lifetime (Tian et al., 2016). The advantage of the system described in this work could be that with an increase of the power to the propeller, the IPS could operate at low temperatures below −10 °C, while no coating has yet been documented that can protect a UAV propeller sufficiently from icing at very cold temperatures. A possible solution that could increase the efficiency of the system could be a combination of electro-thermal anti-icing and a surface coating that reduces the ice adhesion forces to facilitate easier

ice shedding. This has already been proposed for wings (Alamri et al., 2020), and the centrifugal forces by the rotation may assist such a hybrid approach. As none of the described systems works at very low temperatures, the electro-thermal systems, due to power constraints and the coatings because of the increasing ice adhesion forces, a combined system could heat the surface to a lower temperature at which the coating as developed by Han et al. (2022) will then allow an earlier ice shedding.

5. Conclusions

In this paper, an electro-thermal ice protection system for a propeller of a medium-sized fixed-wing UAV was developed. This system was designed using numerical methods based on icing CFD to design the heating zones used in the propeller. Based on those simulations, a propeller with carbon fibre-based heating elements was manufactured. The heating element has two zones separating the heating element into an inner zone with half the heat flux than the outer zone. An electrical power controller powered the IPS to regulate the propeller IPS. As all the modifications to include the IPS are internal to the propeller structure, this system does not affect the performance of the propeller outside of icing conditions, except for friction introduced by the slipring used for the power transfer. This friction is not measured by the dynamometer. This system was tested at three different temperatures at the VTT icing wind tunnel, in both icing and non-icing conditions. The thrust, torque, and rotational rate were recorded during these tests, and the propeller efficiency was calculated. The rotation rate of the propeller was kept constant.

The heated propeller showed the ability to prevent ice accretions to a large extent at −5 °C and to keep an average of more than 93% of the performance of the clean propeller. In contrast, the unheated baseline run would have reduced the propeller's efficiency by 54%. At lower temperatures, the IPS displayed the ability to limit performance degradation. In those conditions, the propeller could not maintain the same high-efficiency level due to ice accumulation on the propeller blades. As a result, the efficiency was reduced by 34% at −10 °C and 65% at −15 °C. This showed that for operations at low temperatures, the IPS needs to be improved to provide more power to the heater or to use the heat more efficiently. In addition to increasing the efficiency of the propeller, the system increased the frequency at which ice shedding events occurred. It thus decreased the mass of ice shedding in every single event. This could decrease the negative effects of ice shedding, like the vibrations caused by uneven ice masses on propeller blades and the risks caused by the ice fragments separating from the propeller that could hit other parts of the UAV.

The method is used to estimate the required heat fluxes yielded power requirements close to the used power levels. However, as the propeller could not be anti-iced at low temperatures, a full calibration of the method was not possible. The analysis of the peak running-wet anti-icing heat fluxes shows the potential for estimating the required anti-icing loads. Overall, this paper proved a concept for a propeller IPS for small fixed-wing UAVs. The proposed system has shown to be suitable to substantially prevent or limit aerodynamic performance degradation in icing condition. The system showed several shortcomings which will be addressed in future development work to further extend efficiency and range of operational temperatures.

Funding

CRediT authorship contribution statement

Nicolas Carlo Müller: Conceptualization, Methodology, Software, Formal-analysis, Validation, Investigation, Data-curation, Writing-original-draft, Visualization. **Bogdan Løw-Hansen:** Investigation, Writing-review-editing. **Kasper Trolle Borup:** Conceptualization, Supervision, Writing-review-editing. **Richard Hann:** Conceptualization, Methodology, Writing-review-editing, Supervision, Project-administration.

Declaration of Competing Interest

The authors declare that they have no known competing financial interests or personal relationships that could have appeared to influence the work reported in this paper.

Data availability

Data will be made available on request.

Acknowledgments

Appendix A Test conditions

Table A4
Test conditions in the IWT during the test campaign. All runs were performed at a velocity of 25 m/s, a rotation rate of 4200 rpm, an LWC of 0.44 g/m^3, and an MVD of 24.2 g/m^3.

Run	IWT Run Number	T	Runtime	IPS power
1	IWT-3–98	−5 °C	240 s	0 W
2	IWT-3–99	−5 °C	240 s	0 W
3	IWT-3–100	−5 °C	240 s	0 W
4	IWT-3–58	−10 °C	240 s	0 W
5	IWT-3–59	−10 °C	240 s	0 W
6	IWT-3–60	−10 °C	240 s	0 W
7	IWT-3–131	−15 °C	240 s	0 W
8	IWT-3–132	−15 °C	240 s	0 W
9	IWT-3–133	−15 °C	240 s	0 W
10	IWT-3–79	−10 °C	600 s	0 W
11	IWT-3–96	−15 °C	600 s	0 W
12	IWT-2–64	−5 °C	180 s	70 W
13	IWT-2–65	−5 °C	180 s	90 W
14	IWT-2–66	−5 °C	180 s	110 W
15	IWT-2–67	−5 °C	180 s	130 W
16	IWT-2–68	−5 °C	180 s	150 W
17	IWT-2–69	−10 °C	180 s	110 W
18	IWT-2–70	−10 °C	180 s	130 W
19	IWT-2–71	−10 °C	180 s	150 W
20	IWT-2–72	−10 °C	180 s	200 W
21	IWT-2–73	−10 °C	180 s	250 W
22	IWT-2–78	−10 °C	600 s	200 W
23	IWT-2–95	−15 °C	600 s	200 W

Appendix B

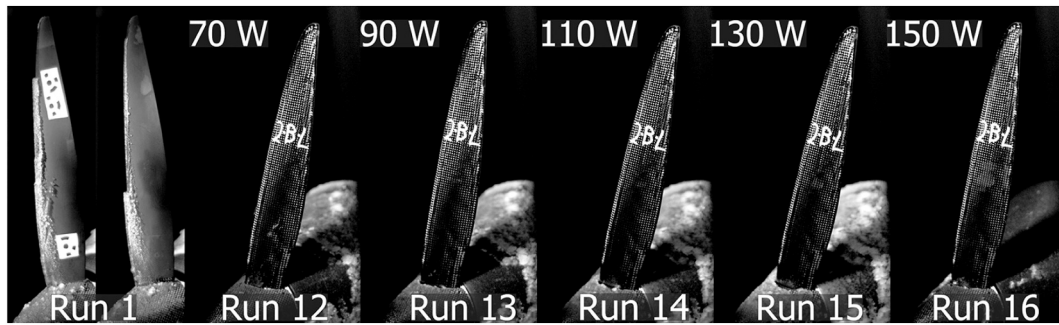**Fig. A20.** High speed camera images of the propeller after 90 s of icing conditions at −5 °C. In all cases, no ice is visible on the propeller.
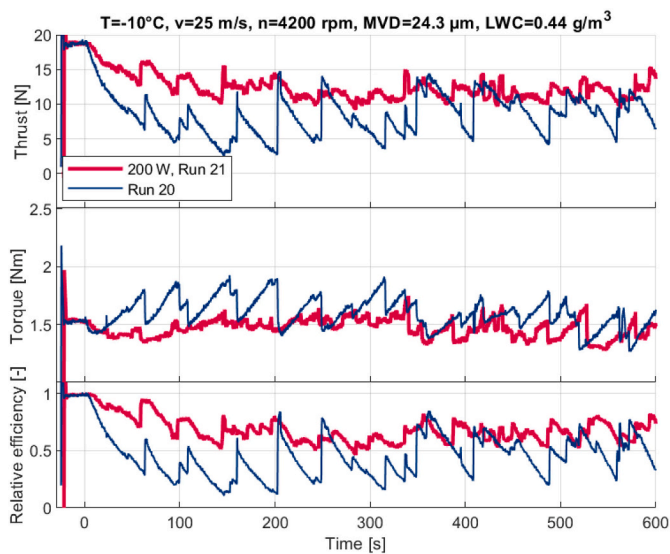
Appendix C

Fig. A21. Change in efficiency of the heated propeller at −10 °C, during a 10 min ice accretion test in the IWT.

References

Adamski, M., 2017. Analysis of propulsion systems of unmanned aerial vehicles. J. Mar. Eng. Technol. 16, 291–297. https://doi.org/10.1080/20464177.2017.1383337.

Alamri, S., Vercillo, V., Aguilar-Morales, A.I., Schell, F., Wetterwald, M., Lasagni, A.F., Bonaccurso, E., Kunze, T., 2020. Self-Limited Ice Formation and Efficient De-Icing on Superhydrophobic Micro-Structured Airfoils through Direct Laser Interference Patterning. Adv. Mater. Interfaces 7, 2001231. https://doi.org/10.1002/admi.202001231 https://onlinelibrary.wiley.com/doi/pdf/10.1002/admi.202001231.

AXI MODEL MOTORS s. r. o.. Axi 5345/16 HD gold line.https://www.modelmotors.cz/product/detail/253/, accessed on 17.01.2023.

Baruzzi, G.S., Habashi, W.G., Guevremont, J.G., Hafez, M.M., 1995. A second order finite element method for the solution of the transonic Euler and navier-stokes equations. Int. J. Numer. Meth. Fluids 20, 671–693. https://doi.org/10.1002/fld.1650200802.

Beaugendre, H., Morency, F., Habashi, W.G., 2003. FENSAP-Ice's three-dimensional in-flight ice accretion module: ICE3D. J. Aircr. 40, 239–247. https://doi.org/10.2514/2.3113.

Beaugendre, H., Morency, F., Habashi, W.G., 2005. Development of a second generation in-flight icing simulation code. J. Fluids Eng. 128, 378–387. https://doi.org/10.1115/1.2169807.

Bourgault, Y., Habashi, W.G., Dompierre, J., Baruzzi, G.S., 1999. A finite element method study of Eulerian droplets impingement models. Int. J. Numer. Meth. Fluids 29, 429–449. https://doi.org/10.1002/(sici)1097-0363(19990228)29:4<429::aid-fld795>3.0.co;2-f.

Bourgault, Y., Habashi, W., Beaugendre, H. 1999. Development of a shallow water icing model in FENSAP-ICE. In: 37th Aerospace Sciences Meeting and Exhibit. doi:10.2514/6.1999-246.

Bourgault, Y., Boutanios, Z., Habashi, W.G., 2000. Three-dimensional eulerian approach to droplet impingement simulation using FENSAP-ICE, part 1: Model, algorithm, and validation. J. Aircr. 37, 95–103. https://doi.org/10.2514/2.2566.

Bragg, M., Broeren, A., Blumenthal, L., 2005. Iced-airfoil aerodynamics. Prog. Aerosp. Sci. 41, 323–362. https://doi.org/10.1016/j.paerosci.2005.07.001.

Cadence Design Systems, Inc., 2023. Pointwise User Manual.https://www.pointwise.com/doc/user-manual/, accessed on 24.01.2023.

Cao, Y., Chen, K., 2010. Helicopter icing. Aeronaut. J. 114, 83–90. https://doi.org/10.1017/S0001924000003559.

Cao, Y., Tan, W., Wu, Z., 2018. Aircraft icing: An ongoing threat to aviation safety. Aerosp. Sci. Technol. 75, 353–385. https://doi.org/10.1016/j.ast.2017.12.028.

Fajt, N., Hann, R., Lutz, T., 2019. The Influence of Meteorological Conditions on the Icing Performance Penalties on a UAV Airfoil. 8th European Conference for Aeronautics and Space Sciences (EUCASS).

Fitzgerald, R., 2007. Wind Tunnel Blockage Corrections for Propellers. University of Maryland.

Gao, M., Hugenholtz, C.H., Fox, T.A., Kucharczyk, M., Barchyn, T.E., Nesbit, P.R., 2021. Weather Constraints on global drone flyability. Sci. Rep. 11. https://doi.org/10.1038/s41598-021-91325-w.

Garner, H.C., Rogers, E., Acum, W., Maskell, E., 1966. Subsonic wind tunnel wall corrections. Technical report. Advisory Group for Aerospace Research and development Neuilly-sur-Seine.

GSVITEC, 2023. High Power LED MULTILED QT.http://www.highspeedimaging.com/wp-content/uploads/2020/04/multiled_qt_abnahme_4.pdf, accessed on 17.01.2023.

GSVITEC, 2023. Multiled G8 key features.https://www.gsvitec.com/multiled-r100/multiled-g8, accessed on 17.01.2023.

Han, N., Hu, H., Hu, H., 2022. An Experimental Investigation to Assess the Effectiveness of Various Anti-Icing Coatings for UAV Propeller Icing Mitigation. In: AIAA AVIATION 2022 Forum. AIAA. https://doi.org/10.2514/6.2022-3964 https://arc.aiaa.org/doi/pdf/10.2514/6.2022-3964.

Hann, R., 2019. UAV icing: Ice accretion experiments and validation. SAE Tech. Pap. Ser. https://doi.org/10.4271/2019-01-2037.

Hann, R., 2020. Atmospheric ice accretions, aerodynamic icing penalties, and ice protection systems on unmanned aerial vehicles, Chapter 7.7. PhD thesis. Norwegian University of Science and Technology.

Hann, R., 2022. UAV Icing: Challenges for computational fluid dynamic (CFD) tools. In: Eleventh International Conference on Computational Fluid Dynamics; ICCFD11.

Hann, R., Johansen, T.A., 2020. Unsettled Topics in Unmanned Aerial Vehicle Icing. SAE Tech. Pap. https://doi.org/10.4271/EPR2020008.

Hann, R., Johansen, T.A., 2021. UAV icing: The influence of airspeed and chord length on performance degradation. Aircr. Eng. Aerosp. Technol. 93, 832–841. https://doi.org/10.1108/aeat-06-2020-0127.

Hann, R., Borup, K., Zolich, A., Sorensen, K., Vestad, H., Steinert, M., Johansen, T., 2019. Experimental Investigations of an Icing Protection System for UAVs. SAE Tech. Pap. Ser. https://doi.org/10.4271/2019-01-2038.

Hann, R., Hearst, R.J., Sætran, L.R., Bracchi, T., 2020. Experimental and Numerical Icing Penalties of an S826 Airfoil at Low Reynolds Numbers. Aerospace 7, 46. https://doi.org/10.3390/aerospace7040046.

Hann, R., Enache, A., Nielsen, M.C., Stovner, B.N., van Beeck, J., Johansen, T.A., Borup, K.T., 2021. Experimental Heat Loads for Electrothermal Anti-Icing and De-Icing on UAVs. Aerospace 8, 83. https://doi.org/10.3390/aerospace8030083.

Hann, R., Enache, A., Nielsen, M.C., Stovner, B.N., van Beeck, J., Johansen, T.A., Borup, K.T., 2021. Experimental Heat Loads for Electrothermal Anti-Icing and De-Icing on UAVs. Aerospace 8, 83. https://doi.org/10.3390/aerospace8030083.

Hann, R., Müller, N.C., Linder, M., Wallisch, J., 2023. UAV Icing: Experimental validation data for predicting ice shapes at low Reynolds numbers (accepted). In: International Conference on Icing of Aircraft, Engines, and Structures.

Hochart, C., Fortin, G., Perron, J., Ilinca, A., 2008. Wind turbine performance under icing conditions. Wind Energy: Int. J. Prog. Appl. Wind Power Conv. Technol. 11, 319–333.

Jokela, T., Tiihonen, M., Karlsson, T., 2019. Validation of Droplet Size in the VTT Icing Wind Tunnel Test Section. In: Proceedings of the Winterwind International Wind Energy Conference.

Karpen, N., Diebald, S., Dezitter, F., Bonaccurso, E., 2022. Propeller-integrated airfoil heater system for small multirotor drones in icing environments: Anti-icing feasibility study. Cold Reg. Sci. Technol. 201, 103616 https://doi.org/10.1016/j.coldregions.2022.103616.

Kontronik, 2023. JIVE Pro 80+ HV JIVE Pro 120+ HV Operation Manual.https://www.kontronik.com/fileadmin/kontronik-sobek/Public/Content/Images/Content/Downloads/Anleitungen/JIVE_Pro.pdf, accessed on 17.01.2023.

Laroche, A., Bottone, D., Seeger, S., Bonaccurso, E., 2021. Silicone nanofilaments grown on aircraft alloys for low ice adhesion. Surf. Coat. Technol. 410, 126971 https://doi.org/10.1016/j.surfcoat.2021.126971.

Liu, Y., Li, L., Li, H., Hu, H., 2018. An experimental study of surface wettability effects on dynamic ice accretion process over an UAS propeller model. Aerosp. Sci. Technol. 73, 164–172. https://doi.org/10.1016/j.ast.2017.12.003.

Liu, Y., Li, L., Ning, Z., Tian, W., Hu, H., 2018. Experimental investigation on the dynamic icing process over a rotating propeller model. J. Propul. Power 34, 933–946. https://doi.org/10.2514/1.B36748.

Liu, Y., Li, L., Chen, W., Tian, W., Hu, H., 2019. An experimental study on the aerodynamic performance degradation of a UAS propeller model induced by ice accretion process. Exp. Thermal Fluid Sci. 102, 101–112. https://doi.org/10.1016/j.expthermflusci.2018.11.008.

Makkonen, L., 2012. Ice Adhesion —Theory, Measurements and Countermeasures. J. Adhes. Sci. Technol. - J ADHES SCI TECHNOL 26, 413–445. https://doi.org/10.1163/016942411X574583.

Mejzlik Propellers s.r.o., 2021. Propeller 21X13 CCW 2B E - Mejzlik Propellers.https://shop.mejzlik.eu/propeller-21x13-ccw-2b-e/, accessed on 2021-11-02.

Messinger, B.L., 1953. Equilibrium temperature of an unheated icing surface as a function of air speed. J. Aeronaut. Sci. 20, 29–42. https://doi.org/10.2514/8.2520.

Meteomatics, 2017. Project "SOPHIA-2" – Final Report: Study of Propeller Icing Hazard in Mini-UAV Aviation. Tech. rep. Meteomatics GmbH.

Müller, N.C., Hann, R., 2022. UAV Icing: A Performance Model for a UAV Propeller in Icing Conditions. In: AIAA AVIATION 2022 Forum. AIAA, pp. 1–17. https://doi.org/10.2514/6.2022-390.

Müller, N.C., Hann, R., 2023. UAV Icing: 3D simulations of propeller icing effects and anti-icing heat loads. In: Proceedings of the International Conference on Icing of Aircraft, Engines, and Structures. SAE International.

Müller, N.C., Hann, R., Lutz, T., 2021. UAV Icing: Numerical Simulation of Propeller Ice Accretion. In: AIAA AVIATION 2021 Forum. AIAA. https://doi.org/10.2514/6.2021-2673 https://arc.aiaa.org/doi/pdf/10.2514/6.2021-2673.

Müller, N.C., Hann, R., Lutz, T., 2021. UAV Icing: Numerical Simulation of Propeller Ice Accretion. In: Proceedings of the AIAA Aviation 2021. American Institute of Aeronautics and Astronautics (AIAA). https://doi.org/10.2514/6.2021-2673.

Nilamdeen, S., Zhang, Y., Ozcer, I., Baruzzi, G.S., 2019. An ice shedding model for rotating components. SAE Tech. Pap. Ser. https://doi.org/10.4271/2019-01-2003.

Papadakis, M., Wong, S.H., Yeong, H.W., Wong, S.C., Vu, G., 2012. Icing Tunnel Experiments with a Hot Air Anti-Icing System. In: 46th AIAA Aerospace Sciences Meeting and Exhibit. AIAA. https://doi.org/10.2514/6.2008-444.

Peck, L., Ryerson, C.C., Martel, C.J., 2020. Army Aircraft Icing. Cold Regions Research and Engineering Laboratory Report.

SAE International, 2015. ARP5905 Calibration and Acceptance of Icing Wind Tunnels. Aerospace Recommended Practice ARP5905.https://doi.org/10.4271/arp5905.

Safran Sensing Technologies Norway AS, 2023. STIM300 Datasheet.https://sensonor.azurewebsites.net/media/5z5lv25o/ts1524-r29-datasheet-stim300.pdf, accessed on 23.02.2023.

Samad, A., Villeneuve, E., Blackburn, C., Morency, F., Volat, C., 2021. An Experimental Investigation of the Convective Heat Transfer on a Small Helicopter Rotor with Anti-Icing and De-Icing Test Setups. Aerospace 8. https://doi.org/10.3390/aerospace8040096.

Shakhatreh, H., Sawalmeh, A.H., Al-Fuqaha, A., Dou, Z., Almaita, E., Khalil, I., Othman, N.S., Khreishah, A., Guizani, M., 2019. Unmanned aerial vehicles (UAVs): A survey on civil applications and key research challenges. Ieee Access 7, 48572–48634.

Szilder, K., McIlwain, S., 2011. In-Flight Icing of UAVs - The Influence of Reynolds Number on the Ice Accretion Process. SAE Tech. Pap. Ser. https://doi.org/10.4271/2011-01-2572.

Szilder, K., Yuan, W., 2017. In-flight icing on unmanned aerial vehicle and its aerodynamic penalties. In: Proceedings of the Progress in Flight Physics, vol. 9, pp. 173–188. doi:10.1051/eucass/2016090173.

Thomas, S.K., Cassoni, R.P., MacArthur, C.D., 1996. Aircraft anti-icing and de-icing techniques and modeling. J. Aircr. 33, 841–854. https://doi.org/10.2514/3.47027.

Tian, X., Verho, T., Ras, R.H., 2016. Moving superhydrophobic surfaces toward real-world applications. Science 352, 142–143. https://doi.org/10.1126/science.aaf2073.

Tiihonen, M., Jokela, T., Makkonen, L., Bluemink, G.J., 2016. VTT icing wind tunnel 2.0. In: Proceedings of the Winterwind International Wind Energy Conference.

Tran, P., Barruzi, G., Tremblay, F., Habashi, W., Petersen, P., Ligget, M., Vos, J., Benquet, P., Fiorucci, S., 2004. FENSAP-ICE applications to unmanned aerial vehicles (UAV). In: 42nd AIAA Aerospace Sciences Meeting and Exhibit. doi:10.2514/6.2004-402.

Inc, T.R. RCBENCHMARK series 1780 test stand - Tyto Robotics, 2023.https://www.tytorobotics.com/pages/series-1780, accessed on 17.01.2023.

Villeneuve, E., Samad, A., Volat, C., Béland, M., Lapalme, M., 2022. Experimental investigation of icing effects on a hovering drone rotor performance. Drones 6, 345. https://doi.org/10.3390/drones6110345.

Vision Research Inc., 2023. Phantom VEO 710.https://www.phantomhighspeed.com/products/cameras/veo/veo710, accessed on 17.01.2023.

Wallisch, J., Hann, R., 2022. UAV Icing: Experimental Investigation of Ice Shedding Times with an Electrothermal De-Icing System. In: AIAA AVIATION 2022 Forum. AIAA, pp. 1–12. https://doi.org/10.2514/6.2022-3905.

Williams, N., Benmeddour, A., Brian, G., Ol, M., 2017. The Effect of Icing on Small Unmanned Aircraft Low Reynolds Number Airfoils. In: 17th Australian International Aerospace Congress: AIAC 2017. Barton; Royal Aeronautical Society, pp. 19–25.

Yan, S., Opazo, T.I., Langelaan, J.W., Palacios, J.L., 2019. Experimental Evaluation and Flight Simulation of Coaxial-rotor Vehicles in Icing Clouds. J. Am. Helicopter Soc.

Yirtici, O., Ozgen, S., Tuncer, I.H., 2019. Predictions of ice formations on wind turbine blades and power production losses due to icing. Wind Energy 22, 945–958. https://doi.org/10.1002/we.2333 https://onlinelibrary.wiley.com/doi/pdf/10.1002/we.2333.

Zhao, G., jun Zhao, Q., Chen, X., 2016. New 3-D ice accretion method of hovering rotor including effects of centrifugal force. Aerosp. Sci. Technol. 48, 122–130. https://doi.org/10.1016/j.ast.2015.10.018.